Characterization and Application of Nanomaterials (2023) Volume 6 Issue 1
doi:10.24294/can.v6i1.2562

ORIGINAL RESEARCH ARTICLE

Nanoscale water flows in networks against a total fail

Sungsook Ahn

Ivy Tech Community College, 200 Daniels Way, Bloomington, IN 47404, USA. E-mail: sungsookahn@yahoo.com

ABSTRACT

A failsafe network design recovering from the stressed condition against a massive supply disruption is generally useful for various applications. Water flow in plants under a tension is inherently vulnerable to an embolism, a water supply cut off, causing a death. However, the function of the network structures of leaf veins and xylem stems effectively reduces the embolism-induced failure. In this study, water transport in plants under the pressurized conditions compared to the normal physiological conditions is observed by X-ray imaing. By examining embolism-induced water supply limits in the architecturally diverse leaf and stem networks, a progressive hydraulic rule has been found: the limited flows in the selected parts of the network structures against a total fail. For a scientific explanation on nanoscale water flow dynamics occurring in plants, temporal meniscus development in the nanomembrane model system is investigated. The pressure-driven hydrodynamic transport phenomena can be explained to follow network dynamics of the modified imbibition typically occuring in nanostrutcures. This study contributes to a variety of design technologies of networked materials against the spread of flow damages under the stressed conditions.

Keywords: Water Flow; Network; Xylem; Leaf Venation; Imbibition

ARTICLE INFO

Received: 11 April 2023
Accepted: 20 May 2023
Available online: 28 May 2023

1. Introduction

The network performance in broad physical[1,2], biological[3] and ecological[4] systems relies largely on the dynamic connection patterns[5,6]. In complex dynamic networks such as power outage[5,7], traffic congestion[8,9], extinction cascade[10,11] and genetic disease[12,13], a local perturbation propagates through a network and reaches a system-specific equilibrium, resulting in a total network failure. Nonetheless, majority of live networks including brain[14] and cellular networks[15] has been reported to generate few catastrophic failures by stable correlations[16–18]. A characteristic of live networks is an evolutionary dynamics to reach an optimum performance. Paradoxically, a compensatory perturbation can direct a network to a desirable state[19]. Well-known examples are a knockdown of a specific gene to recover the strain growth against genetic defects[20], a targeted suppression against extinction of multiple species[19], an appropriate power trimming to reduce subsequent blackouts caused by equipment or operational errors[21,22].

The influences of hydraulic design have been reviewed in terms of the movement of water from roots to leaves of trees[23]. The hydraulic architecture of trees can limit their water relations, gas exchange throughout the crown of trees, the distribution of trees over different habitats and the maximum height that a particular species can achieve. Parameters of particular importance include: (1) the vulnerability of stems to drought-induced cavitation events because cavitation reduces the hydraulic conductance of stems; (2) the leaf specific conductivity of stems because it determines the pressure gradients and most negative water potentials needed to sustain evaporation from leaves; (3) the water storage capacity of tissues because this might determine the ability of trees to survive long drought periods. All of these determining parameters are determined by the optimized structure and function of anatomical components of trees. The dynamic perturbation of network has been observed in the flow systems of plants. Water flows through xylem conduits at a negative pressure by which water is in a metastable state at a risk of cavitation[24,25], resulting in a subsequent loss of xylem function[26]. The hydraulic constraint enables the plant to sacrifice lesser important organs and to save more critical parts for long-term survival and propagation[27]. The susceptibility to an embolism is higher for expendable organs (e.g., leaves) compared with more permanent parts[28]. However, the mechanism and conditional factors of flow limitation against total fail occurring in plants have not yet been clearly understood.

Water ascent through the xylem is driven by the hydrodynamic flow not by the controlled diffusion[29]. Capillary force generated by an evaporation at leaves pulls up water generating a negative pressure[24] by which conduits can cavitate[30]. Further negative pressure in the xylem is promoted by water supply limit such as soil drying. The embolism propagates through the interconnected network by traversing pit membranes between the xylem conduits[31,32]. This drought-induced cavitation occurs via air seeding[26] and is promoted by the pressure difference between gas-filled and water-filled conduits[33]. This cavitation mechanism is more likely than homogeneous nucleation occurring in the bulk phase[34]. On the other hand, refilling process of xylem is more puzzling. It occurs during the daylight thus under a negative tension[35,36]. This result is an apparent paradox against typical understanding where a positive pressure would need to increase the gas solubility restoring back into the sap fluid or pushing out of the conduit[37]. Refilling occurs over a timescale of hours in some species[27,38], but the mechanism is still controversial. The volumetric flow rate is proportional to the fourth power of the xylem size by Hagen–Poiseuille relation[28], thus long and large conduits are advantageous for water flow[28,39,40]. Nonetheless, the water flow in a stem has not been considered as a network dynamics working by cooperative adoption of conduits in a bundle. Leaf network has been naturally evolved for a long history to maximize flow efficiency against embolism[41–43]. However, little is known about the dynamic adoption of leaf networks and refilling after the embolism to avoid the catastrophic failure.

High hydraulic tension in xylem is prone to exogenous embolism during the manipulation thus typical intrusive measurements unable the studies on the water supply initiation and embolism propagation in plants under the increased stress[37]. However, *in-situ* imaging techniques such as X-ray, magnetic resonance and neutron have provided new insights[31,44–49]. Air seeding has been directly visualized by synchrotron X-ray imaging in this point[44,48]. The limited resolution and possible damage by ionizing radiation have been overcome in micro- and nano-imaging technologies[46–49]. Effectively utilizing gold nanoparticle (AuNP), isotope chemical tracer or water-air interface as an imaging contrast, water transport in plants has been successfully traced with minimum sample damage. Here, water movement in plants is observed by synchrotron X-ray imaging and the suggested physical phenomena is reenacted by nanomembrane model systems. An explanation has been developed first to our knowledge for the water flow network dynamics under the stressed condition and refilling mechanism. The resultant knowledge is important for the understanding the plant mortality over a drought which is the results of natural selection[41] and for the providing useful engineering solutions for failsafe network designs[50] in diverse applications such as effective fluid delivery[51], energy distribution[52], and data communication[53].

2. Results

Water movement in the xylem vessels of a stem. Water flows in the xylem and phloem bundles of

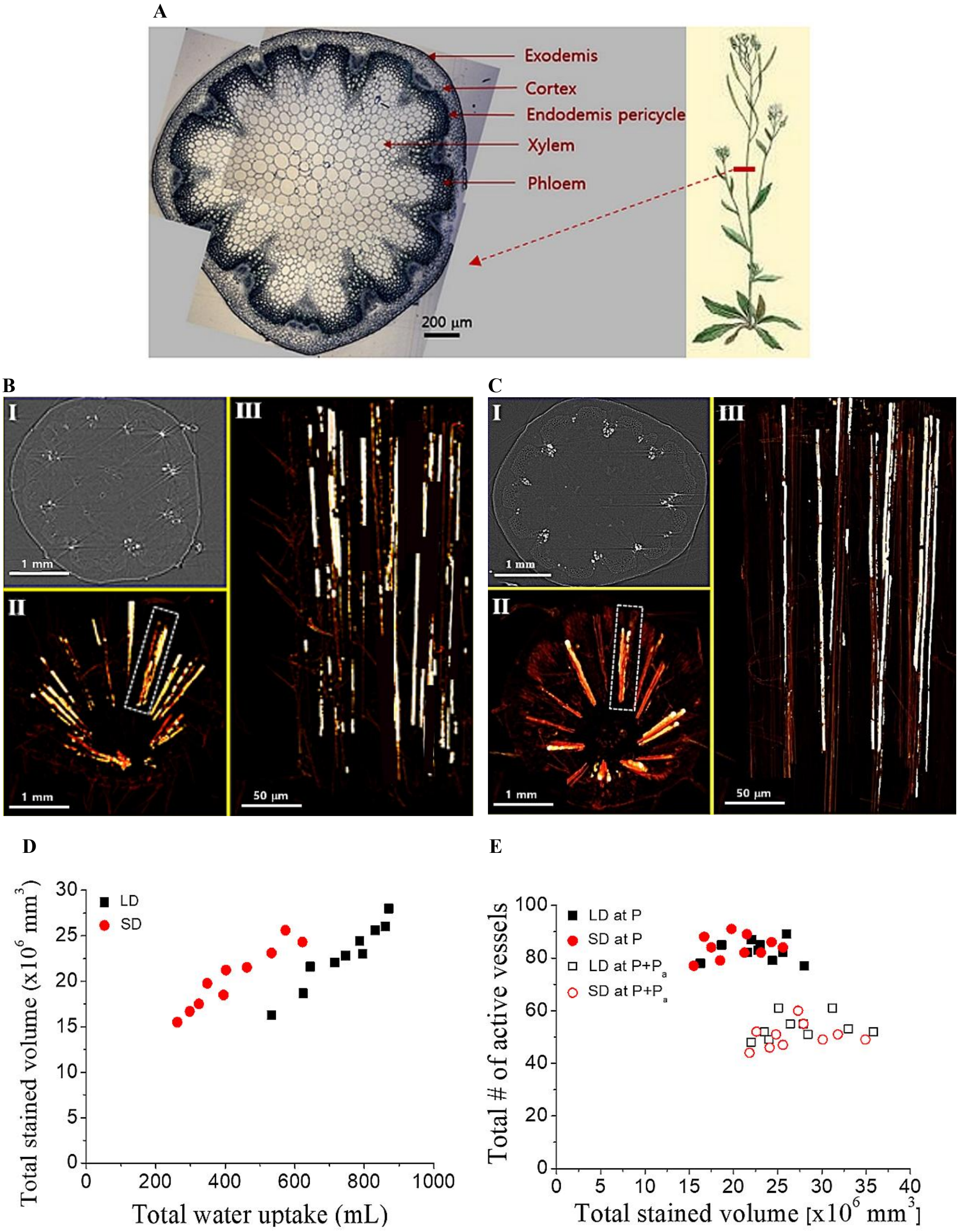

Figure 1. (A) X-ray image of the *Arabidopsis* stem cut. Cross-sectional images are obtained by X-ray computed tomography (X-ray CT). **(B)** The projected images of stem cut Arabidopsis obtained by X-ray microscopy (XM) [I] and axially accumulated into 3D images [II]. The image of the bundle marked by a white rectangle in [II] is magnified in [III]. Water moves up naturally by the physiological self-action of the plant under the normal condition where a cut is dipped in the AuNP containing aqueous culture medium. **(C)** Water moves up by the additionally introduced negative pressure in an *Arabidopsis* stem cut. **(D)** Water uptake of *Arabidopsis* grown in long day (LD) and short day (SD) condition is evaluated in terms of the stained volume by the AuNP. The samples grown in LD condition display higher water uptake than those of SD condition. But each system shows linear relation of water uptake with stained volume. **(E)** Total number of active xylem vessels in an *Arabidopsis* stem is similar regardless of total stained volume for both normal pressure (P) and additionally introduced pressure ($P + P_a$) conditions. The total number of active vessels has no strong relation with the total water uptake. However the number of active vessels used under the additionally introduced negative pressure ($P + P_a$) shows less number than normal pressure condition (P).

Arabidopsis are experimentally observed (**Figure 1A**) for which X-ray imaging is employed using gold nanoparticle (AuNP) tracer[46–49]. Xylem vessels are divided into three types according to the water uptake efficiency: The xylem vessels filled with stationary water, embolized vessels due to low water uptake and AuNP-stained vessels induced by active water uptake. The water uptake efficiency occurring in a plant is in strong relation with the structural pathways of the water movement. In this point, the interconnected microstructural networks in a bundle are investigated[54] for which the location of the active xylems of high water uptake is determined by the AuNP-stained vessels[46,47] (**Figure 1B**,**C**). Water movement in a stem is investigated by cross-sectional 2D images [I] which are axially accumulated into 3D images [II]. A representative bundle marked by a white dotted rectangle in [II] is magnified in [III]. First, water moves up in a stem cut by a physiological self-action under the typical pressure (P) natural in a plant (**Figure 1B**). Stained by AuNPs, many short tracks are dispersed in an axial direction in addition to the vertical water flow tracks. The water movement pathway in natural physiological condition (P) is spatially broad across the vessels. Second, additional negative pressure is introduced ($P + P_a$ where both P & $P_a < 0$) at a rate of –0.002 μL/min to a stem cut (Methods) and modified water flow pattern is investigated (**Figure 1C**). When an additional negative pressure is applied the water moves in straight long lines in fewer number vessels (point-selection) compared with the normal pressure condition in **Figure 1B**. Especially, the number of active vessels in a bundle decreases. It is noticeable that the increased pressure is related with the flow pattern change into straight long lines limited in the selected active points.

The water movements in *Arabidopsis* stems are graphically analyzed by the X-ray images. The total volume of active xylem vessels evaluated by AuNP stain is in strong relation with total water uptake (**Figure 1D**). The total volume of water uptake is determined by the remaining solution in the vials at 10 min intervals. All water uptake experiments are carried out in the chamber in which plants were grown at two growth conditions: long day (LD) and short day (SD). The total stained volume is linearly proportional to the total water uptake for each growth condition. Overall, the LD condition generates high water uptake over the SD condition with similar stained volume, indicating faster flow rate. On the other hand, the total number of active vessels (AuNP-stained vessels) of both LD and SD condition is independent of total stained volume (**Figure 1E**). Under the normal physiological pressure condition (P), both LD and SD show total number of active vessels between 70 to 90. Meanwhile, the total number of active vessels counted under the additional negative pressure condition ($P + P_a$) is between 40 to 60. The total stained volume under the additional pressure condition ($P + P_a$) is slightly larger than normal pressure condition (P), thus less number of vessels transport more water. In summary, under the pressurized condition, the water flow in a stem is limited in some points. This is one survival strategy of plant segmentation as a compensatory perturbation of network dynamics. The flow pattern generates more straight lines with less meandering, thus it is more advantageous for more effective water delivery in a short time duration.

Water movement in the xylem vessels of a leaf. As a systematically designed network structure, leaves with different venations are investigated. The vein structure typically possesses a hierarchy of vein orders[55,56]. The lower-order veins are major veins, thus one or more 1st order veins run from the petiole to the leaf apex. Meanwhile, 2nd order veins branch at intervals and 3rd order veins branch between. From lower to higher vein orders, cross-sectional areas of the xylems and phloems typically decrease[57–59]. A hierarchy of vein orders typically forms a reticulate mesh[56,60]. This is determined by the looping where the end points of higher order veins link back to the lower order ones. In this study, three different venation structures are investigated (**Figure 2**): 1st order veins are colored in black lines, 2nd order veins in red lines and 3rd order veins in blue lines both in the schemes at the left and in the graphs at the right. *Privet* has a reticulate venation with 3rd order hierarchy (**Figure 2A**), *Rhapis Excelsa* a reticulate

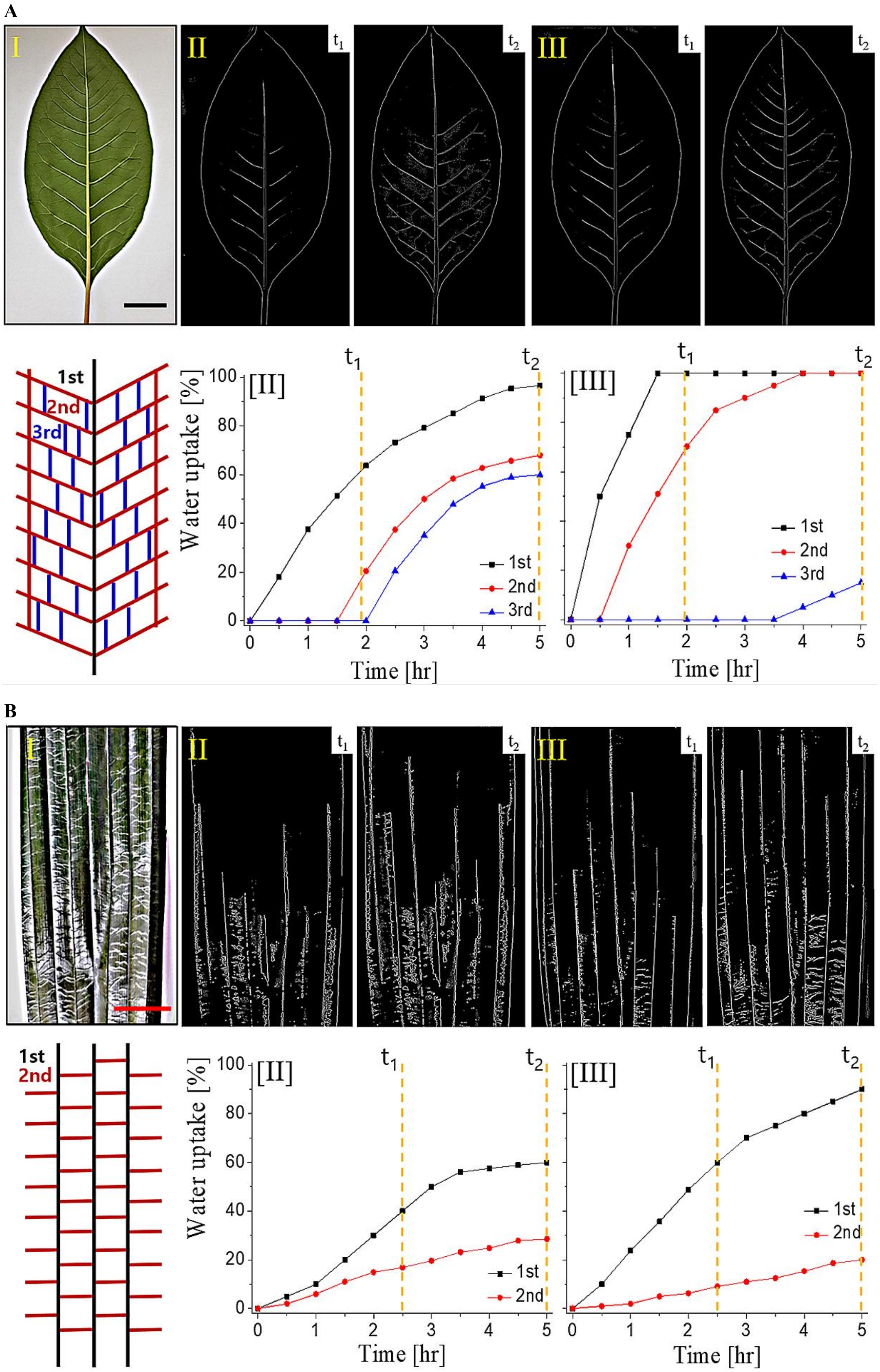

Figure 2. (*Continued*).

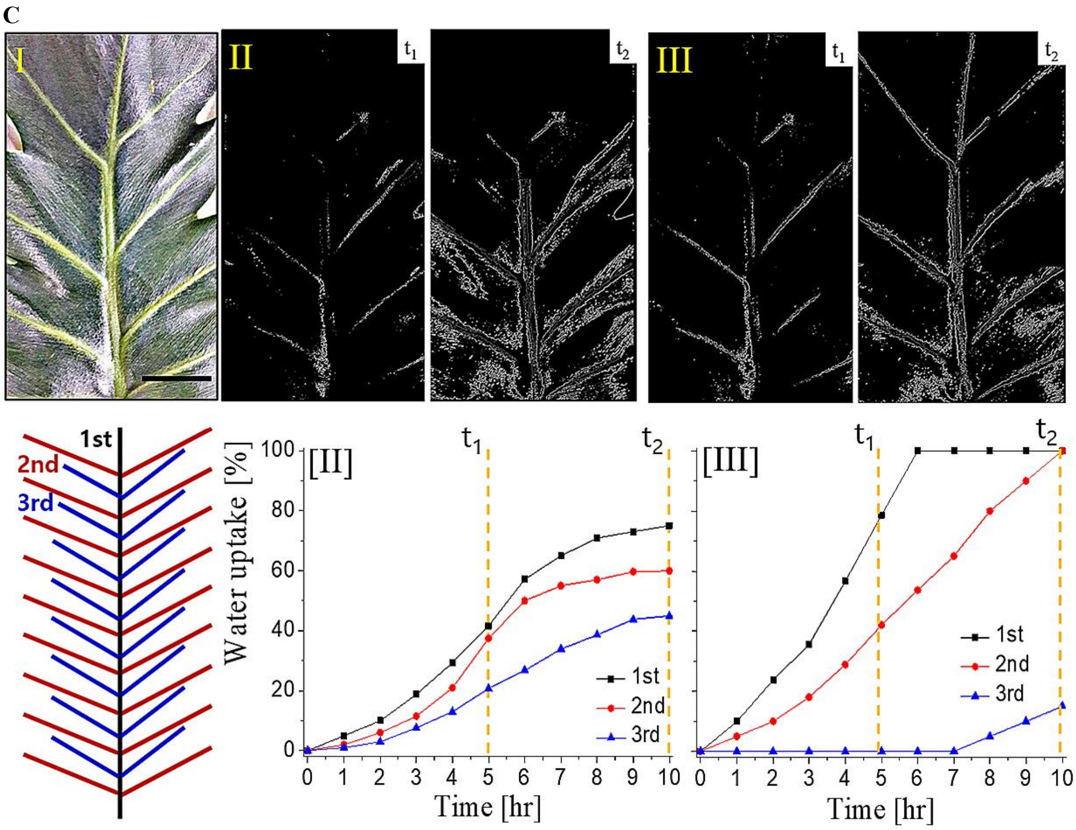

Figure 2. The leaves with different venation structures observed by the optical microscopy and X-ray microscopy (XM) images for **(A)** Reticulate venation (*Privet*) with 3rd order hierarchy. **(B)** Reticulate venation (*Rhapis Excelsa*) with 2nd order hierarchy. **(C)** Nonreticulate venation (*Ficus lutea*) with 3rd order hierarchy. The scale bar in the optical microscopy image [I] is 1 cm. Time-dependent XM images are captured consecutively and representative images at two interval t_1 and t_2 are displayed in [II] & [III]. The newly introduced Iopamidol aqueous solution is traced against the water already existing in the veins under normal pressure condition at water-water interface [II] and under increased negative pressure by dried condition at water-air interface [III]. Time-dependent water filling into the veins is graphically analyzed under the corresponding XN image according to the hierarchy of the vein structure.

venation with 2nd order hierarchy (**Figure 2B**), and *Ficus lutea* a nonreticulate (open) venation with 3rd order hierarchy (**Figure 2C**). To clarify the anatomical morphology of the venation, optical microscopy images [I] are arranged together. The contrast in the X-ray image can be generated by water-air interface, Iopamidol or AuNP aqueous solution[46–49]. In this study Iopamidol aqueous solution shows the best result for leaf venation observation. By combining small patches captured in different regions, a whole picture of the microscale X-ray image is obtained at two different time interval t_1 [II] and t_2 [III]. The newly introduced Iopamidol aqueous solution is traced against already existing water in the leaf veins under the normal physiological condition (P) generating water-water interface [II]. In addition to the normal pressure condition, additional negative pressure is introduced ($P + P_a$) inside the veins by drying the samples [III] (Methods). Filling the xylems by air reduces water transport and further increases xylem tension[61]. Matric potential (Ψ_m) is the amount of water bound to the matrix of a plant via hydrogen bonds and is always negative to zero. In a dried plant it can be as low as −2 MPa while it is as high as zero in a water-saturated state[61]. The water movement in dried leaves is traced at the water-air interface by which the water filling in the highest order veins is displayed as white lines.

Temporal water movement of reticulate venation with 3rd order hierarchy (*Privet*) (**Figure 2A**) shows that Iopamidol aqueous solution fills the 1st order main vein at the center, and spreads to the 2nd and 3rd order veins. The temporal vein filling is graphically investigated for each XM image. It is expressed by the % of whole veins at a hierarchy order for which the % of the vein is determined by total vein length estomated by optical microscopy. At the water-saturated normal condition [II], the veins close to the petiole and the higher order veins are filled together without fully filling the entire lower order veins. On the other hand, the Iopamidol solution fills the veins of the dried samples in different ways [III]. With additionally applied negative pressure generated by drying ($P + P_a$) and by making water-air interface, Iopamidol aq. solution fully fills the lower order main veins first and then moves to the higher order veins. Fluid traced images of *Rhapis Excelsa* a reticulate venation with 2nd order hierarchy with multiple 1st order veins, also display time-dependent water filling through hierarchically ordered veins (**Figure 2B**). In the fully watered samples [II] the veins close the petiole are first filled rather than filling entire 1st order main veins. Meanwhile, in the dried sample [III], the lower order main veins are first filled significantly. *Ficus lutea* a nonreticulate thus open venation with 3rd order hierarchy (**Figure 2C**) also shows more effective main vein filling under the dried state. Regardless of the venation structure, hierarchical water filling of the lower order main veins preferentially occurs under the high pressure condition ($P + P_a$), while distance from the water source is important for the vein filling at normal pressure condition (P). In terms of venation-specific water flow difference, *Rhapis Excelsa* with 2nd order hierarchy with multiple 1st order veins can be more advantageous for effective water filling under a stressed condition. Nonetheless, the number of orders and the degree of reticulation seems not the determining factors to decide the water flow tracks. The water flow in a leaf under the pressurized condition is limited preferably for the main veins according to the hierarchy. This also can be considered as one of the plant segmentation phenomena as a compensatory perturbation of network dynamics.

Nanoscale water movement model system. Water movement in model systems is investigated by cellulose acetate nanomembranes (surface free energy, $\gamma_s = 52.6$ mJ/m^2)[62] (Chmlab Co., Barcelona, Spain) with 200 nm (I) and 800 nm (II) pore size (provided by Chmlab Co.). The structure is visualized and the average pore size is confirmed by X-ray nanoimaging (**Figure 3A**)[63,64]. Rhodamine B aqueous solution of low concentration (1 ppm) clearly visualizes the flow tracks in red, which continuously moves filling the nanopores. Moving distance of this clear-cut meniscus vs. time is measured to obtain the flow rate by taking movie clips (10 fps speed). To trace the regionally diversified meniscus location as a sharp point, membranes are linearly folded (0.2 cm in span). Flows through the membranes are evaluated in three arrangement (**Figure 3B**): first, water flow from the bottom to the top of the membrane against the gravity ($-P_g$, P_g is the pressure induced by the gravity) generates the typical spontaneous imbibition [I]. A part of the membrane is still dipped in the Rhodamine B aqueous solution, so that water is continuously provided without any level change of the container. Second, the membrane is horizontally placed where the gravity effect on the meniscus movement in the membrane is minimized [II]. The meniscus change is analyzed from the line where horizontal water movement starts. In the third position, water flows from the top to the bottom thus it is accelerated by the gravity ($+P_g$) [III]. The meniscus movement is analyzed from the line where the vertical water movement starts. For each case in **Figure 3B**, representative meniscus movements in a membrane traced by red color are displayed as an inset. For safe meniscus recording, the data is collected from 30 sec after the dipping so that rapid invasion of water into the pores is not considered. In addition, by the unavoidable Rhodamine B mass transfer even at very low concentration and natural water evaporation from the membranes surface, the final meniscus becomes a dark red line because of the Rhodamine B accumulation by the Marangoni effect[64]. But this is hardly observed when the flow moves dynamically thus the time-dependent meniscus movement is recorded before this phenomena becomes serious.

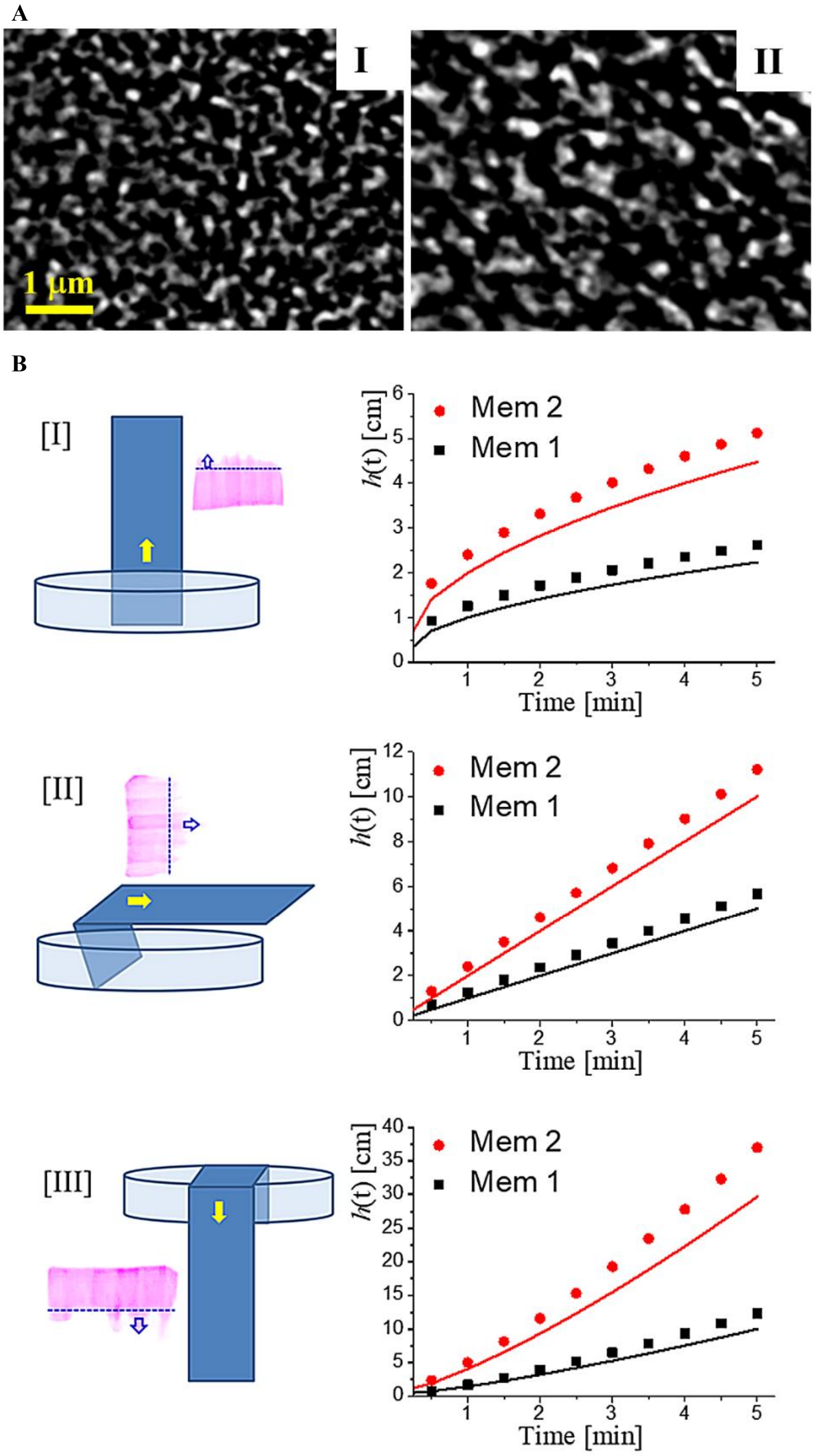

Figure 3. (*Continued*).

C

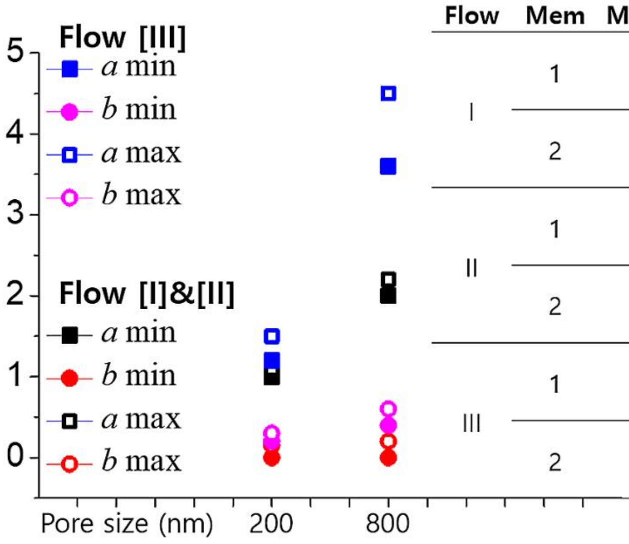

Flow	Mem	Meniscus	*a*	*b*	*n*
I	1	min	**1**	**0**	0.5
		max	1.1	0.15	0.5
	2	min	2	0	0.5
		max	2.2	0.2	0.5
II	1	min	1	0	1
		max	1.1	0.15	1
	2	min	2	0	1
		max	2.2	0.2	1
III	1	min	1.2	0.2	1.3
		max	1.5	0.3	1.3
	2	min	3.6	0.4	1.3
		max	4.5	0.6	1.3

Figure 3. (A) X-ray nanoscopy (XN) image of the cellulose acetate nanomembranes with average pore size of 200 (I) and 800 nm (II). Rhodamine B aqueous solution is used for visualization of newly introduced flow against already existing fluid. **(B)** Flow through the membrane is evaluated in three position: [I] The water flows from the bottom to the top against the gravity ($-P_g$). [II] The membrane is horizontally placed so that gravity effect is minimized. [III] Water flows from the top to the bottom thus accelerated by the gravity ($+P_g$). For each case representative meniscus movement in a membrane is displayed on which the dotted baseline represents the minimum position of the meniscus while the fastest point marked by an arrow represents the maximum distance from the baseline. The flows through the two membranes (Mem 1 and Mem 2) are graphically investigated at the right of each flow type. Lines represent the baseline of the minimum meniscus while symbols indicate the fastest point. **(C)** Time-dependent meniscus position, $h(t)$ follows power law dependency by $h(t) = at^n + b$. Based on this relation, the results in Fig 3B are fitted by least squares fitting method ($R^2 > 0.99$). The fitting parameters are summarized in a table and graphical comparison of *a* and *b* values are displayed at the left.

For the quantitative flow analysis at the right graphs, the degree of meniscus development is considered in this study rather than average meniscus position. Two time-dependent tracking points are focused in this aspect: one is the time-dependent base line (lines in the membrane at the left and in the graph at the right) representing the minimum position of the meniscus. From this line, each flow point of the membrane is diversified by the local flow rate difference. The other is the fastest moving point (arrows in the membrane and solid symbols in the graph). Running faster from the base line it represents the maximum position of the meniscus.

Flows through the two membranes of different pore size are graphically summarized. The pore size of the membrane I (Mem 1) is four times smaller than that of membrane II (Mem 2). This is accompanied by three suggested flow types from [I] to [III]. The penetration length, $h(t)$ during a time is considered by the spontaneous imbibition of water into hydrophilic porous structures. The absolute $h(t)$ value significantly increases from flow [I] to [III], and time-dependent flow rate (slope of the graph) is also prominently increases in that order. Especially large pore size Mem 2 shows higher values than those of smaller pore size Mem 1 in every case.

Power-law dependency on the time. The $h(t)$ by the spontaneous imbibition follows the scaling law of Lucas-Washburn[64,65],

$$h(t) = (tr\sigma_{LV}\cos\theta/2\eta)^{1/2} \quad (1)$$

η: dynamic viscosity,
r: effective pore size,
σ_{LV}: liquid-vapor surface tension,
θ: contact angle.

Although both capillarity and gravity forces exist in spontaneous imbibition, gravity is not included in Lucas-Washburn relation, which causes a deviation from the half-power dependency on the time[66–68]. In addition, there are intermediate stages before and after the typical Lucas-Washburn regime, where the half-power time dependency is not effective any more[69–71]. At the very beginning of water contact with a membrane, the water invades to the porous media in a radical manner, by which the meniscus moves in linear relation with the elapsed time, $h(t) \sim t$. Meanwhile, at the very late period of spontaneous imbibition, gravitational force significantly overcomes the capillary dynamics, $h(t) < t^{1/2}$.

For the flows arranged in **Figure 3B**, time-dependent meniscus position from the water source, $h(t)$ follows power law dependency on the time which is generalized as

$$h(t) = at^n + b \tag{2}$$

n reflects the power law-dependent flow mechanism. a is the multiplication factor diversified by the structure and compatibility of the media and viscosity of the moving fluid. Meanwhile, b is the addition factor considering added forces such as forced diffusion, gravity and the like. In all three membrane arrangement, large pore size Mem 2 shows high $h(t)$ values both for the minimum baseline (lines) and the maximum fastest point (solid symbols). Based on the general power law relation, the results are demonstrated by least squares fitting within a reasonable error range ($R^2 > 0.99$) (**Figure 3C**). The fitting parameters are arranged in a table. The a and b values are graphically compared at the left, which are same for flow [I] and [II] while those of flow [III] increases significantly. The a and b values obtained by the flow [I] through the Mem 1 at the baseline position are used as calibration factor (1 and 0, respectively, bold characters in the table). Therefore, the values for other conditions are normalized in the table by these two multiplication and addition factors. In a typical imbibition against gravity in flow [I], fitting by $n = 0.5$ is applied. Compared with baseline, the fastest point shows slightly increased a values both for Mem 1 (1.1/1.0) and Mem 2 (2.2/2.0). In terms of the pore size effect, the a values reflect 2 times faster movement in Mem 2 than Mem 1 based on both minimum (2.0/1.0) and maximum (2.2/1.1) position of the meniscus. This corresponds to the expected value by the relation of $h(t) \sim (r)^{1/2}$. In this condition, the b values for fastest point increases to 0.15 and 0.2 for Mem 1 and Mem 2, respectively, while the b values for the base lines are all zero. This indicates that no additional force is employed for the baseline movement. However, additional force is generated to the fastest point movement and this is pore size-dependent. This makes the difference (even though it is slight) between the fastest point and the baseline in spontaneous imbibition.

In a horizontal movement with minimized gravity [II], $n = 1$ is effective. This indicates different mechanism of the flow [II] with minimized gravity compared with the flow [I] against gravity. However, the a and the b values are same with those of the flow [I], indicating no additional modification or added force to the flow when the membrane is posed in horizontal direction. On the other hand, in a vertical movement accelerated by the gravity in [III], $n = 1.3$ is properly fitted. Compared with flow [I], a values for baseline increases 1.2 times (1.2/1.0) for Mem 1 and 1.7 times (3.6/2.0) for Mem 2. Meanwhile, for the fastest point, a values increases 1.4 times (1.5/1.1) for Mem 1 and more than 2 times (4.5/2.2) for Mem 2. Therefore, flow increase is more prominent for the fastest point than the baseline. In terms of the pore size effect, the a values of Mem 2 are three times larger than those of Mem 1 both for baseline (3.6/1.2) and fastest point (4.5/1.5), satisfying the relation, $h(t) \sim (r)^{4/5} > (r)^{1/2}$. Therefore, the pore size dependency becomes more significant for flow [III] than the flow [I] and [II]. Compared with zero values for the flow [I] and [II], the b values of flow [III] increases to 0.2 (Mem 1) and 0.4 (Mem 2) for baseline, indicating size-dependent additional force generation by the vertical flow. This becomes 1.5 times larger for fastest points as 0.3 (Mem 1) and 0.4 (Mem 2) respectively. Therefore, added gravity significantly affects additional force generation which is more prominent for fastest point than baseline. And this becomes more prominent for larger pore size.

In any flow type occurring in a complex network, there is a meniscus development making minimum and maximum position. This might depend on the local geometry difference: there is a more advantageous point for the flow in the media such as large pore and direct shortcut flow path etc., which can make stronger connection in a network. This difference becomes more significant with large pore size and additional force introduction. In a spontaneous imbibition, the arrangement of flow direction multiplies the flow rate. This is affected by the pore size of the media, flow mechanism and additionally added pressures. Prominently, the flow at the fastest point away from the baseline increases significantly by an additionally added pressure ($+P_g$). This can be one supporting information where some selected points in a network takes faster flow.

3. Discussion

New insights for the imbibition. Spontaneous imbibition is important not only for its fundamental aspects but also for its special applications in liquid penetration into nano materials[67], ink penetration in paper or coating on paper[72], oil recovery where gas/oil is displaced by a different liquid[73], and the like. In the spontaneous imbibition the mean advancing front is known to follow Lucas-Washburn's law[74,75]. For this the behavior of $h \sim t^{1/2}$ is followed, which also has been reported with other similar models[66,67]. Nonetheless, the one-half power scaling law is not always effective with other factors affected by property of fluids and media[67,68,73]. The effect of gravity on spontaneous imbibition in porous media investigated both theoretically and experimentally[77], shows that the spontaneous imbibition can be governed by the hydraulic conductivity (permeability) of the porous media. In addition, few study has focused on the scientific explanation of the local meniscus development rather than using mean values. By the aforementioned water movement mechanisms occurring in nanomembrane models, the fluid flows in a complex nanoporous network structure are observed to follow the power dependency on the time, $h(t) = at^n + b$. Depending on the time-dependent mechanism, power dependency n as well as magnitude a and additive b values are modified. It is experimentally observed that for a spontaneous imbibition $n = 0.5$ is satisfied however when gravity effect is minimized $n = 1$ is effective. In addition, with added gravity, $n > 1$ is satisfied. Therefore, half-power time dependency is not the criteria to explain the imbibition mechanism in which water fills the nano-scale structures spontaneously. In addition, multiplication and addition factors are observed to strongly depend on the membrane pore size and added forces.

The way of water movement by spontaneous imbibition is also sensitively modified by the geometry of the porous media. Imbibition is a dynamic procedure limited in the situation where water moves by forming an air-water interface. The variation of mass (m) during the time (t) by the spontaneous imbibition of water into hydrophilic porous structures follows the Lucas-Washburn scaling law[64,65],

$$m(t) = C\sqrt{t},\ C = \rho \boldsymbol{A} \Phi \sqrt{(r\, \sigma_{LV} \cos\theta / 2\tau\eta)} \tag{3}$$

ρ: density of the fluid
η: dynamic viscosity
$\boldsymbol{A}$: cross-sectional area of the sample
Φ: pore volume fraction
r: effective pore radius
σ_{LV}: liquid-vapor surface tension
θ: contact angle
$\boldsymbol{\tau}$: tortuosity

The main structural contribution, $\boldsymbol{\tau}$ describes the connectivity and meandering of the pores[78]. The meandering of the pores increases the length of the flow path hence increases $\boldsymbol{\tau}$. Therefore, by locally differentiated thus smaller $\boldsymbol{\tau}$, water flows with minimized meandering and effective transportability.

The water permeation under a pressure gradient contains a filtration constant, elastic modulus of the media, and osmotic concentration. When a pressure is applied to a vessel channel, the free energy of water is isothermally raised by $V\Delta P$, where V is the volume of water in the sample and ΔP is the pressure increase necessary to establish an equilibrium between water in and out of the system. In the water movement by capilarity, the water flows through smooth walled capillaries, where the volumetric flow rate ($\mathrm{d}V/\mathrm{d}t$) is proportional to the applied pressure gradient by the distance l ($\mathrm{d}P/\mathrm{d}l$) mediated by the hydraulic conductivity ($K_{\text{capillary}}$), $\mathrm{d}V/\mathrm{d}t = -K_{\text{capillary}}(\mathrm{d}P/\mathrm{d}l)$, (the minus sign indicates the water flow from high to low pressure). The $K_{\text{capillary}}$ is then proportional to the fourth power of the capillary size : $K_{\text{capillary}} = r^4\pi/8\eta$, where η is the dynamic viscosity of fluid (Pa.s). This pressure-induced Hagen-

Poiseuille based capillarity relation displays strong media size-dependency of water movement through pipe-like channels. Therefore, when a pressure is further loaded over the normal condition (addition factor *b* value increase) Hagen-Poiseuille based capillarity become significant. This condition is more sensitively affected by the pore size ($\sim r^4$).

Other spontaneous movement of water is diffusion (even though water flow in a plant is not considered in this category) which follows the Fick's law[79–81]. Water enters the free space of a medium, surrounds and diffuses into each subunit overcoming the diffusion barriers. The kinetics of this diffusion follows Fick's first law, $\partial C_i/\partial t = D\boldsymbol{A}(C_0 - C_i)/Vh$, ($C_i$: concentration of moving molecules in the media; C_0: external concentration, D: the diffusion coefficient of in the media; V: the volume of the media; $\boldsymbol{A}$: the area through which the diffusion is taking place; h: the distance of the diffusion). On the other hand, water enters and diffuses continuously through uniformly distributed resistance. Such diffusion into a sheet would follow Fick's second law, yielding a time course relation of $C_i/\partial t = D(\partial^2 C_i/\partial h^2)$[82]. Inhirently diffusion is not driven by the forced action but a result of the random movement of molecules. However, considering the concentration difference of the water molecules, water-air interface is more advantageous for fast movement than water-water condition in any of diffusion condition.

Point-selection and faster movement. In the time-dependent $\Delta h(t)$ value change for two Mem 1 and Mem 2 tracked in red in the membrane, the flow of a specific point is far faster than baseline movement (**Figure 4A**). The time-dependent difference between the minimum baseline and the maximum fastest point is indicated by $\Delta h(t)$ for three flow types [I] to [III]. This quantifies a specific point movement faster than other local fluid body tracks even though it also follows same power law dependency with baseline track. Overall, the absolute value of $\Delta h(t)$ is large in the order of flow [I] < flow [II] < flow [III], indicating effective acceleration by additionally introduced forces such as gravity. In addition, large pore size Mem 2 shows higher $\Delta h(t)$. For every case, time-dependent change, $d\Delta h(t)/dt$ strongly depends on the flow type in the order of flow [I] < flow [II] < flow [III]. From the graphical investigation of three flow types, Mem 2 generates higher $\Delta h(t)$ value in flow [III] prominently.

Survival strategy of the live systems. In a graphical summary at the right (re-graphed from **Figure 2A**), for the dried samples ($P + P_a$, solid symbol lines) the lower order veins are more effectively filled out in a fast way than those under the normal physiological pressure (P, empty symbol lines) (**Figure 4B**). This is explained by additionally added pressure ($P + P_a$) loaded on the water flow mechanism which is more sensitive for point-selected faster movement. The phenomena are also observed in membrane model system where the spontaneous imbibition is modified as summarized in **Figure 4A**.

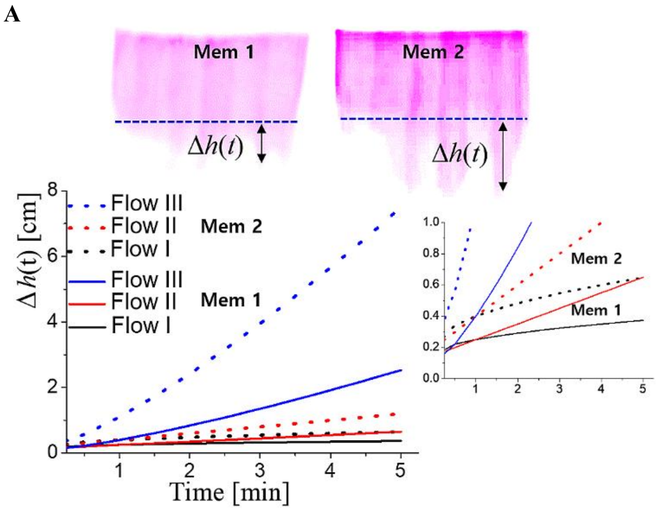

Figure 4. (*Continued*).

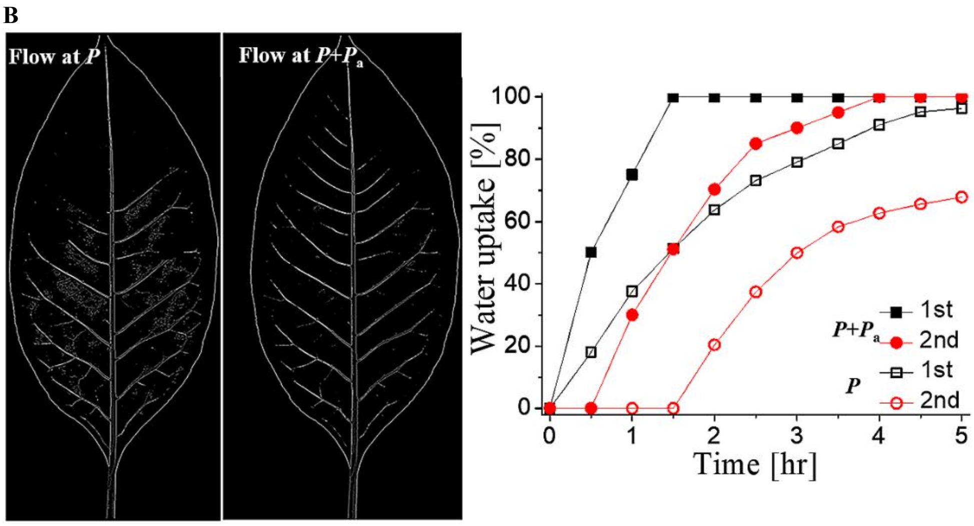

Figure 4. **(A)** The time-dependent difference between the minimum baseline and the maximum fastest point expressed by Δ$h(t)$ for three flow types [I] to [III] with two Mem 1 (solid lines) and Mem 2(dotted lines). **(B)** Water uptake profile of a selected venation structure is arranged by X-ray image at the left and analyzed graph are the right. At normal pressure condition (P, empty symbol lines) and additional pressure condition ($P + P_a$, solid symbol lines).

4. Conclusion

As an important survival strategy the important main veins of a plant is filled out first under the water deficient stressed condition. By this way, water can be provided for more urgent parts first. The way of transport phenomena adopted by the live system is one of the naturally adopted strategies for a long evolution history. In this study, compensatory perturbations of network dynamics and the concept of plant segmentation are discussed as a related apparent phenomenon. The science behind is water flow mechanism affected by many conditional factors. Water movements observed in plant systems are explained in conjunction with model systems. As a result, it is confirmed that specific structures enhances the water flow and this is favorably performed by the appropriate physical factors such as pressure vs. flow in the structure.

5. Methods

Synchrotron X-ray micro imaging (XM). XM images of plants were obtained at the 6C Biomedical Imaging beamline at the Pohang Ligh Source II (PLS II, Pohang, South Korea). For the X-ray computed tomography (X-ray CT) scanning, the plants were rotated in the X-ray white beam from 0 to 180° by the increments of 0.5° yielding two-dimensionally projected images which are accumulated into 3D images. Each projection was magnified through an objective lens and relayed onto a 4,008 × 2,600 pixel CCD camera (Vieworks). These raw 2D tomographic projections were reconstructed into 1340 TIF image slices using Octopus 8.3 software (Institute for Nuclear Science). These images were analysed in Amira 5.2 software. First, the white beam allows X-ray image acquisition with high spatial and temporal resolutions. To reduce potential damages to live samples, additional 1 mm-thick aluminium plates were used to remove most X-rays below 10 keV. A CCD camera (Vieworks, VM-2M35) with 1,600 × 1,200 pixels provides magnified images by a 5 × objective lens (field-of-view (FOV) = 2,083 × 1,563 μm^2) or a 10 × objective lens (FOV = 1,013 × 759 μm^2). X-ray images were consecutively captured at 10 to 20 frames per second (fps), with an exposure time of 60 to 100 ms. A safe time limit of 20 s was set for continuous imaging of a given experimental set-up to avoid possible damage to the live tissues. Generally, the objective lens with low magnification (5×) was used for the long-distance tracking of the water/air menisci through the vessel elements. The 10× objective lens was used to precisely visualize the anatomical structure. Second, the monochromatic beam (10 keV X-ray) was used to trace sap movement for an extended period (longer than 5 min for total exposure) as well as to minimize potential damage to the live samples. A 1,024 × 1,024 pixel CCD camera (Redlake, MegaPlusII ES2001) was used to capture

X-ray images at 24 fps, with an exposure time of 30 ms (FOV=735 × 735 μm^2 with a 10 × objective lens or FOV = 2,219 × 2,219 μm^2 with a 4× objective lens).

Synchrotron X-ray nanoscopy (XN). Experiments were carried out at the 7C beamline at PLS II. The X-ray source of 10^{11} photons/μm^2/sec consists of undulator with 20 mm period and 70 poles. The beam size is about 100 μm × 100 μm at 7 keV. The X-ray source was radiated from a 3 GeV bending magnet and then monochromatized using a Ge (111) DCM. To achieve focused images, monochromatic X-ray beam was focused on the sample using a condenser zone-plate (CZP, 1 mm dia. Beryllium refractive compound lenses) with innermost and outermost diameters of 4 nm and 100 nm, respectively. The primary X-ray image was magnified 50 times with an objective zone plate lens (140 μm innermost and 50 nm outermost diameter, W). It was then converted into a visible image on a thin scintillator crystal (Tb: LSO, 20 μm thickness). The visible image was further magnified ×20, using an optical microscope. This provides a total ×1,000 magnification of image on a cooled CCD camera (Princeton Instrument VersArray 1300B cooled CCD) of 1,340 × 1,300 pixels, which corresponds to an equivalent FOV of 21 × 21 μm^2 with 30 nm resolution.

Plant sample preparation. *Arabidopsis* seeds were germinated in an incubator at 30 °C. After 3 days, the germinated seeds were transferred to a hydroponic culture system and grown in a greenhouse (16/8 hr photoperiod at 300 $\mu mol\ m^{-2}\ s^{-1}$, 27/22 °C day/night, 50%–60% humidity) up to the flag leaf stage (approximately 7 weeks). The culture solution (pH 6) contains (mM): $KH_2PO_4 = 0.21$, $K_2HPO_4 = 0.06$, $KNO_3 = 1.98$, $Ca(NO_3)_2 = 2.96$, $MgSO_4 = 0.61$, $(NH_4)_2SO_4 = 0.53$, $MnSO_4 = 2.9 \times 10^{-3}$, $ZnSO_4 = 2.5 \times 10^{-3}$, $KCl = 0.1$, $(NH_4)_2MoO_4 = 6 \times 10^{-5}$, $CuSO_4 = 6.3 \times 10^{-2}$, $H_3BO_3 = 7.4 \times 10^{-3}$, and EDTA-Fe=0.206. All the plant samples prepared for X-ray observation were collected from well-watered plants early in the morning to ensure low levels of native embolism. Branches were collected in the morning half an hour before the experiment. To prevent an invasion of air from the cut edge of the plant, vessel lengths were measured by air-injection, and branches were cut more than two times longer than the longest vessel. All measurements were performed on the leaves at the distal ends of these cut branches. Plants of different leaf venation, *Privet*, *Ficus lutea* and *Rhapis Excelsa* were purchased[83] in a soil pot and used without further treatment. The leaves attached to a sprig were used. The samples were cut and dipped in an Iopamidol solution (0.1% m/m) to keep water-water interaction. After XM observation, the same samples were dipped in the media solution for 12 hr for stabilization. And then the samples were taken out of the media and left for 12 hr to generate water-air interface in the veins. These dried samples were dipped in the Iopamidol solution during the XM observation. During the venation observation, due to limited FOV, small patches were put together to complete one whole image of a large size. For this, an exposure time was limited no longer than 3 sec at a time and focus region was carefully controlled without unnecessary exposure of samples to the beam.

Negative pressure generation. Artificial negative pressure was applied using a syringe pump (remote Infuse/Withdraw PHD Ultra 4400 Programmable Syringe Pumps, Harvard Apparatus, USA). The upper cut end of stem sections or branches were connected to the syringe via a silicon tube and the negative pressure was monitored using a cell pressure probe. The pressure value, i.e. the gauge pressure, was maintained at approximately −0.1 MPa throughout the experiments. For negative pressure generated onto a stem cut, an air-tight plastic tube was tightly connected. After link to the syringe pump, negative pressure was controlled by withdrawing mode at a −0.002 μL/min speed. Pressure probe technique (Der Werkzeugmacher) was adopted to control water suction mode in a plant. Negative pressure in the leaves with three different venations was generated by drying each sample for 12 hrs. The dried state was confirmed by using ImageJ to detect the embolism events from the previous water-saturated X-ray image sequence. To increase the difference between noise and the embolized region, a smoothing filter was applied. Next, threshold was applied to the image sequence, that maximizes the embolized region and minimizes the noise.

Water movement in xylem vessels in a stem. Water movement in a stem occurs in a complex structure. *Arabidopsis Thaliana* is employed with two different genotypes (Ler and Clv3) and growth conditions (long-day, LD and short-day, SD) as a live model system. Gold nanoparticle (AuNP) aqueous solution is employed to trace sap fluid movement in a stem and observed by X-ray microscopy (XM) computed tomography (**Figure A1**)[46,47]. Xylems and phloems in bundles are investigated by rendering the cross-sectional 2D images into 3D images (**Figure 1A**). In terms of the total number of xylem vessels, the genotype Clv3 has more vessels over Ler (**Figure A2**). However, active vessels (AuNP-stained vessels) are not much differentiated by the genotypes, while the growth condition (LD and SD) generates noticeable difference. Therefore, Arabidopsis (Ler) of LD and SD conditions are selected in this study for water flow observation. In addition to typical axial flow, radial flow is generated by the interconnection of pores among the adjacent xylems within a bundle (**Figure A3**). For this process a stem cut is dipped in an aqueous culture medium containing concentration-controlledAuNP (~20 nm diameter, 2.4×10^{21} AuNP/m^3).

Acknowledgments

The authors are grateful for the valuable help in the experiments performed at the Pohang Light Source II (PLS-II, Pohang, South Korea) utilizing X-ray micro imaging (XM) at 6C beamline and X-ray nanoimaging (XN) at 7C beamline.

Conflict of interest

The author declares no conflict of interest.

References

1. Carreras BA, Lynch VE, Dobson I, Newman DE. Critical points and transitions in an electric power transmission model for cascading failure blackouts. Chaos 2002; 12(4): 985–984. doi:10.1063/1.1505810.
2. Motter AE. Cascade control and defense in complex networks. Physical Review Letters 2004; 93(9): 098701. doi: 10.1103/PhysRevLett.93.098701.
3. Cornelius SP, Lee JS, Motter AE. Dispensability of *Escherichia coli*'s latent pathways. Proceedings of the National Academy of Sciences 2011; 108(8): 3124–3129. doi: 10.1073/pnas.1009772108.
4. Sahasrabudhe S, Motter AE. Rescuing ecosystems from extinction cascades through compensatory perturbations. Nature Communications 2011; 2(1): 170. doi: 10.1038/ncomms1163.
5. Buldyrev SV, Parshani R, Paul G, *et al.* Catastrophic cascade of failures in interdependent networks. *Nature* 2010; 464(7291): 1025–1028. doi: 10.1038/nature08932.
6. Leicht EA, D'Souza RM. Percolation on interacting networks. arXiv 2009; arXiv:0907.0894. doi: 10.48550/arXiv.0907.0894.
7. Carreras BA, Newman DE, Dobson I, Poole AB. Evidence for selforganized criticality in a time series of electric power system blackouts. IEEE Transactions on Circuits and Systems I: Regular Papers 2004; 51(9): 1733–1740. doi: 10.1109/TCSI.2004.834513.
8. Helbing D. Traffic and related self-driven many-particle systems. Reviews of Modern Physics 2001; 73(4): 1067. doi: 10.1103/RevModPhys.73.1067.
9. Vespignani A. Predicting the behavior of techno-social systems. Science 2009; 325(5939): 425–428. doi: 10.1126/science.1171990.
10. Pace ML, Cole JJ, Carpenter SR, *et al.* Trophic cascades revealed in diverse ecosystems. Trends in Ecology and Evolution 1999; 14(12): 483–488. doi: 10.1016/S0169-5347(99)01723-1.
11. Scheffer M, Carpenter S, Foley JA, *et al.* Catastrophic shifts in ecosystems. Nature 2001; 413(6856): 591–596. doi: 10.1038/35098000
12. Motter AE. Improved network performance via antagonism: From synthetic rescues to multi-drug combinations. Bioessays 2010; 32(3): 236–245. doi: 10.1002/bies.200900128.
13. Barabási AL, Gulbahce N, Loscalzo J. Network medicine: A network based approach to human disease. Nature Reviews Genetics 2011; 12(1): 56–68. doi: 10.1038/nrg2918.
14. Dosenbach NUF, Fair DA, Miezin FM, *et al.* Distinct brain networks for adaptive and stable task control in humans. Proceedings of the National Academy of Sciences 2007; 104(26): 11073–11078. doi: 10.1073/pnas.0704320104.
15. Vidal M, Cusick ME, Barabási AL. Interactome networks and human disease. Cell 2011; 144(6): 986–998. doi: 10.1016/j.cell.2011.02.016.
16. Pastor-Satorras R, Vázquez A, Vespignani A. Dynamical and correlation properties of the Internet. Physical Review Letters 2001; 87(25): 258701. doi: 10.1103/PhysRevLett.87.258701.
17. Gallos LK, Song C, Makse HA. Scaling of degree correlations and its influence on diffusion in scale-free networks. Physical Review Letters 2008;

100(24): 248701. doi: 10.1103/PhysRevLett.100.248701.

18. Radicchi F. Driving interconnected networks to supercriticality. Physical Review X 2014; 4(2): 021014. doi: 10.1103/PhysRevX.4.021014.
19. Cornelius SP, Kath WL, Motter AE. Realistic control of network dynamics. Nature Communications *2*013; 4(1): 1942. doi: 10.1038/ncomms2939.
20. Motter AE, Gulbahce N, Almaas E, Barabási AL. Predicting synthetic rescues in metabolic networks. Molecular Systems Biology 2008; 4(1): 168. doi: 10.1038/msb.2008.1.
21. Dobson I, McCalley J, Liu CC. Fast simulation, monitoring, and mitigation of cascading failure. Tempe: Power Systems Engineering Research Center (PSERC) Publication; 2010.
22. Anghel M, Werley KA, Motter AE. Stochastic model for power grid dynamics. In: Proceedings of the 40th International Conference on System Sciences (HICSS'07); 2007 Jan 3–6; Waikoloa, HI, USA. IEEE; 2007. p. 113.
23. Tyree MT, Ewers FW. The hydraulic architecture of trees and other woody plants. New Phytologist 1991; 119(3): 345–360. doi: 10.1111/j.1469-8137.1991.tb00035.x.
24. Wheeler TD, Stroock AD. The transpiration of water at negative pressures in a synthetic tree. Nature 2008; 455(7210): 208–212. doi: 10.1038/nature07226.
25. Da Silva VR. Hydraulic conductivity. London: IntechOpen; 2013.
26. Tyree MT, Sperry JS. Vulnerability of xylem to cavitation and embolism. Annual Review of Plant Biology 1989; 40: 19–38. doi: 10.1146/annurev.pp.40.060189.000315.
27. Zimmermann MH. The hydraulic architecture of plants. In: Xylem structure and the ascent of sap. New York: Springer-Verlag; 1983. p. 66–82.
28. Tyree MT, Ewers FW. The hydraulic architecture of trees and other woody plants. New Phytologist 1991; 119(3): 345–360. doi: 10.1111/j.1469-8137.1991.tb00035.x.
29. Zimmermann MH, Brown CL. Trees: Structure and cunction. New York: Springer-Verlag; 1971.
30. Hacke U, Sauter JJ. Drought-induced xylem dysfunction in petioles, branches and roots of Populus balsamifera and Alnus glutinosa (L.) Gaertn. Plant Physiology 1996; 111(2): 413–417. doi: 10.1104/pp.111.2.413.
31. Brodersen CR, McElrone AJ, Choat B, *et al.* In vivo visualizations of drought-induced embolism spread in *Vitis vinifera*. Plant Physiology 2013; 161(4): 1820–1829. doi: 10.1104/pp.112.212712.
32. Tyree MT, Sperry JS. Do woody plants operate near the point of catastrophic xylem dysfunction caused by dynamic water stress?: Answers from a model. Plant Physiology 1988; 88(3): 574–580. doi: 10.1104/pp.88.3.574.
33. Pittermann J, Choat B, Jansen S, *et al.* The relationships between xylem safety and hydraulic efficiency in the Cupressaceae: The evolution of pitMembrane form and function. Plant Physiology 2010; 153(4): 1919–1931. doi: 10.1104/pp.110.158824.
34. Pockman WT, Sperry JS, O'Leary JW. Sustained and significant negative water-pressure in xylem. Nature 1995; 378(6558): 715–716. doi: 10.1038/378715a0.
35. Brodersen CR, McElrone AJ, Choat B, *et al.* The dynamics of embolism repair in xylem: In vivo visualizations using high resolution computed tomography. Plant Physiology 2010; 154(3): 1088–1095. doi: 10.1104/pp.110.162396.
36. Martorell S, Diaz-Espejo A, Medrano H, *et al.* Rapid hydraulic recovery in *Eucalyptus pauciflora* after drought: Linkages between stem hydraulics and leaf gas exchange. Plant, Cell & Environment 2014; 37(3): 617–626. doi: 10.1111/pce.12182.
37. Wheeler JK, Huggett BA, Tofte AN, *et al.* Cutting xylem under tension or supersaturated with gas can generate PLC and the appearance of rapid recovery from embolism. Plant, Cell & Environment 2013; 36(11): 1938–1949. doi: 10.1111/pce.12139.
38. Zwieniecki MA, Melcher PJ, Ahrens ET. Analysis of spatial and temporal dynamics of xylem refilling in Acer rubrum L. using magnetic resonance imaging. Frontiers in Plant Science 2013; 4: 265. doi: 10.3389/fpls.2013.00265.
39. Steudle E, Peterson CA. How does water get through roots? Journal of Experimental Botany 1998; 49(322): 775–788. doi: 10.1093/jxb/49.322.775.
40. Ewers FW, Carlton MR, Fisher JB, *et al.* Vessel diameters in roots versus stems of tropical lianas and other growth forms. IAWA Journal 1997; 18(3): 261–279.
41. Sperry JS, Love DM. What plant hydraulics can tell us about responses to climate-change droughts. New Phytologist 2015; 207(1): 14–27. doi: 10.1111/nph.13354.
42. Boyce CK, Brodribb TJ, Feild TS, Zwieniecki MA. Angiosperm leaf vein evolution was physiologically and environmentally transformative. Proceedings of the Royal Society B: Biological Sciences 2009; 276(1663): 1771–1776. doi: 10.1098/rspb.2008.1919.
43. Brodribb TJ, Feild TS. Leaf hydraulic evolution led a surge in leaf photosynthetic capacity during early angiosperm diversification. Ecology Letters 2010; 13(2): 175–183. doi: 10.1111/j.1461-0248.2009.01410.x.
44. Choat B, Brodersen CR, McElrone AJ. Synchrotron X-ray microtomography of xylem embolism in *Sequoia sempervirens* saplings during cycles of drought and recovery. New Phytologist 2015; 205(3): 1095–1105. doi: 10.1111/nph.13110.
45. Hochberg U, Albuquerque C, Rachmilevitch S, *et al.* Grapevine petioles are more sensitive to drought induced embolism than stems: Evidence from *in vivo* MRI and microcomputed tomography observations of hydraulic vulnerability

segmentation. Plant, Cell & Environment 2016; 39(9): 1886–1894. doi: 10.1111/pce.12688.

46. Ahn S, Jung SY, Lee JP, *et al.* Gold nanoparticle flow sensors designed for dynamic X-ray imaging in biofluids. ACS Nano 2010; 4(7): 3753–3762. doi: 10.1021/nn1003293.
47. Park J, Kim HK, Ryu J, *et al.* Functional water flow pathways and hydraulic regulation in the xylem network of Arabidopsis. Plant and Cell Physiology 2015; 56(3): 520–531. doi: 10.1093/pcp/pcu198.
48. Ryu J, Ahn S, Kim SG, *et al.* Interactive ion-mediated sap flow regulation in olive and laurel stems: Physicochemical characteristics of water transport via the pit structure. PLoS One 2014; 9(5): e98484. doi: 10.1371/journal.pone.0098484.
49. Hwang BG, Ahn S, Lee SJ. Use of gold nanoparticles to detect water uptake in vascular plants. PLoS One 2014; 9(12): e114902. doi: 10.1371/journal.pone.0114902.
50. Boccaletti S, Latora V, Moreno Y, *et al.* Complex networks: Structure and dynamics. Physics Reports 2006; 424(4–5): 175–308. doi: 10.1016/j.physrep.2005.10.009.
51. Case DJ, Liu Y, Kiss IZ, *et al.* Braess's paradox and programmable behaviour in microfluidic networks. Nature 2019; 574(7780): 647–652. doi: 10.1038/s41586-019-1701-6.
52. Albert R, Albert I, Nakarado GL. Structural vulnerability of the North American power grid. Physical Review E 2004; 69(2): 025103. doi: 10.1103/PhysRevE.69.025103.
53. Cohen R, Erez K, ben-Avraham D, Havlin S. Resilience of the internet to random breakdowns. Physical Review Letters 2000; 85(21): 4626–4628. doi: 10.1103/PhysRevLett.85.4626.
54. Zwieniecki MA, Melcher PJ, Feild TS, Holbrook NM. A potential role for xylem–phloem interactions in the hydraulic architecture of trees: Effects of phloem girdling on xylem hydraulic conductance. Tree Physiology 2004; 24(8): 911–917. doi: 10.1093/treephys/24.8.911.
55. Esau K. Anatomy of seed plants. 2nd ed. New York: John Wiley & Sons; 1977.
56. Hickey LJ. Classification of architecture of dicotyledonous leaves. American Journal of Botany 1973; 60(1): 17–33. doi: 10.2307/2441319.
57. Plymale EL, Wylie RB. The major veins of mesomorphic leaves. American Journal of Botany 1944; 31(2): 99–106. doi: 10.2307/2437600.
58. Coomes DA, Heathcote S, Godfrey ER, *et al.* Scaling of xylem vessels and veins within the leaves of oak species. Biology Letters 2008; 4(3): 302–306. doi: 10.1098/rsbl.2008.0094.
59. Sack L, Scoffoni C, McKown AD, *et al.* Developmentally based scaling of leaf venation architecture explains global ecological patterns. Nature Communications 2012; 3(1): 837. doi: 10.1038/ncomms1835.
60. McKown AD, Cochard H, Sack L. Decoding leaf hydraulics with a spatially explicit model: Principles of venation architecture and implications for its evolution. The American Naturalist 2010; 175(4): 447–460. doi: 10.1086/650721.
61. Transport of water and solutes in plants. Available from: https://courses.lumenlearning.com/boundless-biology/chapter/transport-of-water-and-solutes-in-plants/.
62. van Oss CJ. Interfacial forces in aqueous media. 2nd ed. New York: CRC Press; 2006.
63. Lee SJ, Kim K, Ahn S. The internal structure of macroporous membranes and transport of surface-modified nanoparticles. Microscopy and Microanalysis 2015; 21(4): 936–945. doi: 10.1017/S1431927615013719.
64. Gruener S, Huber P. Imbibition in mesoporous silica: Rheological concepts and experiments on water and a liquid crystal. Journal of Physics: Condensed Matter 2011; 23(18): 184109. doi: 10.1088/0953-8984/23/18/184109.
65. Gruener S, Sadjadi Z, Hermes HE, *et al.* Anomalous front broadening during spontaneous imbibition in a matrix with elongated pores. Proceedings of the National Academy of Sciences 2012; 109(26): 10245–10250. doi: 10.1073/pnas.1119352109.
66. Li K, Horne RN. Generalized scaling approach for spontaneous imbibition: An analytical model. SPE Reservoir Evaluation & Engineering 2006; 9(3): 251–258. doi: 10.2118/77544-PA.
67. Supple S, Quirke N. Rapid imbibition of fluids in carbon nanotubes. Physical Review Letters 2003; 90(21): 214501. doi: 10.1103/PhysRevLett.90.214501.
68. Soriano J, Mercier A, Planet R, *et al.* Anomalous roughening of viscous fluid fronts in spontaneous imbibition. Physical Review Letters 2005; 95(10): 104501. doi: 10.1103/PhysRevLett.95.104501.
69. de Gennes PG, Brochard-Wyart F, Quere D. Hydrodynamics of interfaces: Thin films, waves, and ripples. In: Capillarity and wetting phenomena: Drops, bubbles, pearls, waves. New York: Springer; 2004.
70. Quéré D. Inertial capillarity. Europhysics Letters 1997; 39(5): 533–538. doi: 10.1209/epl/i1997-00389-2.
71. Huber P. Soft matter in hard confinement: Phase transition thermodynamics, structure, texture, diffusion and flow in nanoporous media. Journal of Physics: Condensed Matter 2015; 27(10): 103102. doi: 10.1088/0953-8984/27/10/103102.
72. Miranda AM, Menezes-Sobrinho IL, Couto MS. Spontaneous imbibition experiment in newspaper sheets. Physical Review Letters 2010; 104(8): 086101. doi: 10.1103/PhysRevLett.104.086101.
73. Li K, Horne RN. Computation of capillary pressure and global mobility from spontaneous water imbibition into oil-saturated rock. SPE Journal 2005; 10(4): 458–465. doi: 10.2118/80553-PA.
74. Washburn EW. The dynamics of capillary flow. Physical Review 1921; 17(3): 273–283. doi: 10.1103/PhysRev.17.273.
75. Lucas R. On the time law of the capillary rise of liquids. Kolloid-Zeitschrift 1918; 23(1): 15.

76. Xue Y, Markmann J, Duan H, *et al.* Switchable imbibition in nanoporous gold. Nature Communications 2014; 5(1): 4237. doi: 10.1038/ncomms5237.
77. Li K, Zhang D, Bian H, *et al.* Criteria for applying the Lucas-Washburn law. Scientific Reports 2015; 5(1): 14085. doi: 10.1038/srep14085.
78. Bernabé Y, Li M, Maineult A. Permeability and pore connectivity: A new model based on network simulations. *Journal of Geophysical Research: Solid Earth* 2010; 115: B10203. doi: 10.1029/2010JB007444
79. Bear J. Dynamics of fluids in porous media. Elsevier; 1972.
80. Bonner J. Water Transport: This classical problem in plant physiology is becoming increasingly amenable to mathematical analysis. Science 1959; 129: 447–450.
81. Kim ME, Jeoung DJ, Kim KS. Effects of water flow on dental hard tissue ablation using Er:YAG laser. Journal of Clinical Laser Medicine & Surgery 2003; 21(3): 139–144. doi: 10.1089/104454703321895581.
82. Szafer A, Zhong J, Gore JC. Theoretical model for water diffusion in tissues. Magnetic Resonance in Medicine 1995; 33(5): 697–712. doi: 10.1002/mrm.1910330516.
83. Available from: http://www.knrrc.or.kr/ (accessed 2023 May 1).

Appendix

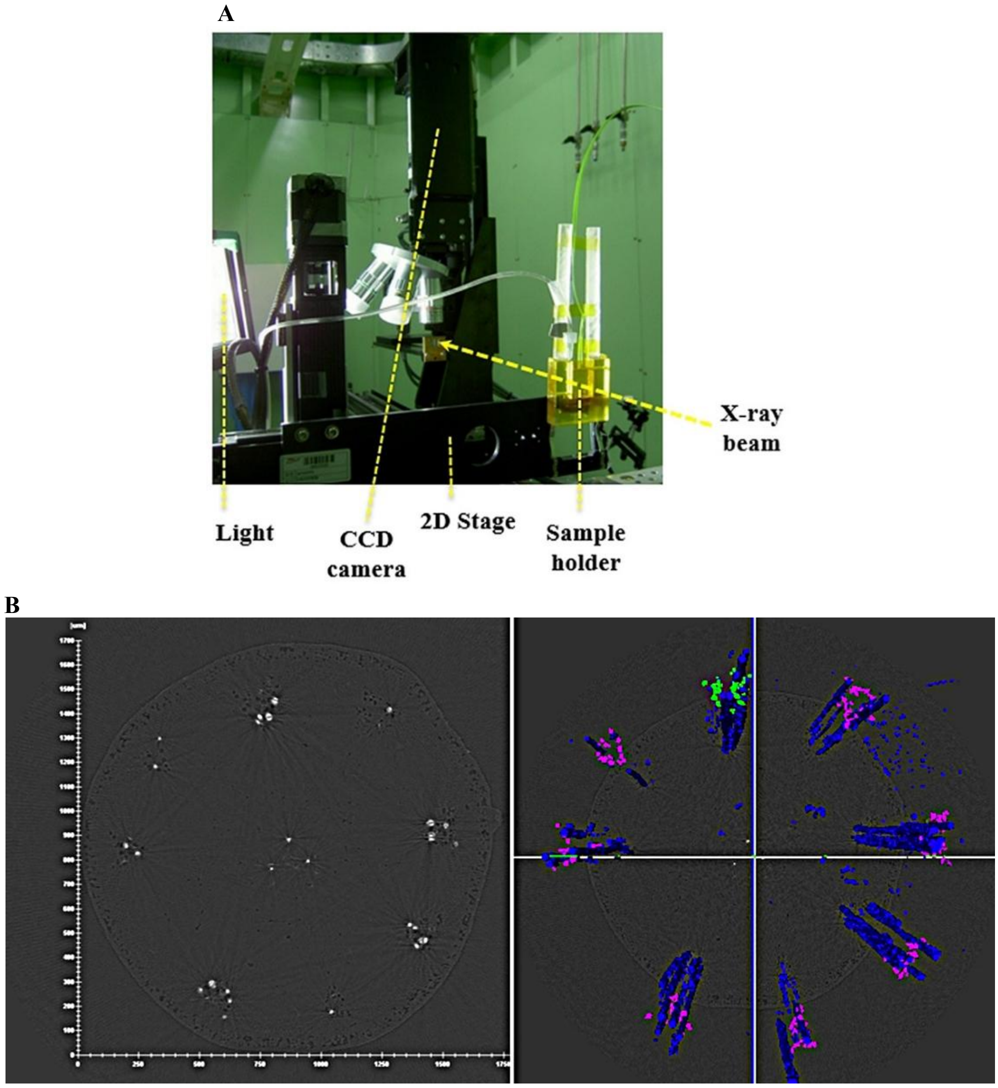

Figure A1. Water uptakes in *Arabidopsis Thaliana* has been investigated by two different genotypes (*Ler* and *Clv3*) and growth conditions (long day, LD and short day, SD): **(A)** X-ray imaging set-up at the 6C beamline of PAL (Pohang, South Korea). **(B)** Gold nanoparticle stained X-ray microscopy (XM) computed tomography 2D images (left) which are accumulated into 3D image (right).

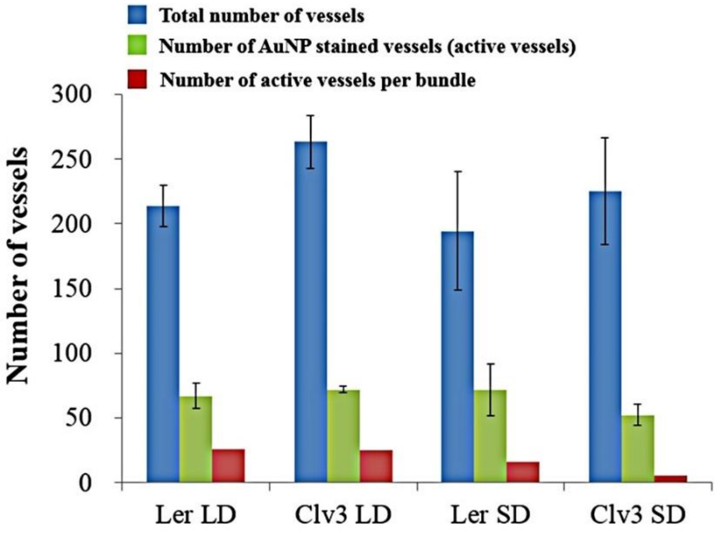

Figure A2. Xylem vessel types of *Arabidopsis* are evaluated. Total number of xylem vessels, AuNP-stained xylem vessels and number of xylem vessels per bundle are counted for each genotypes and growth condition.

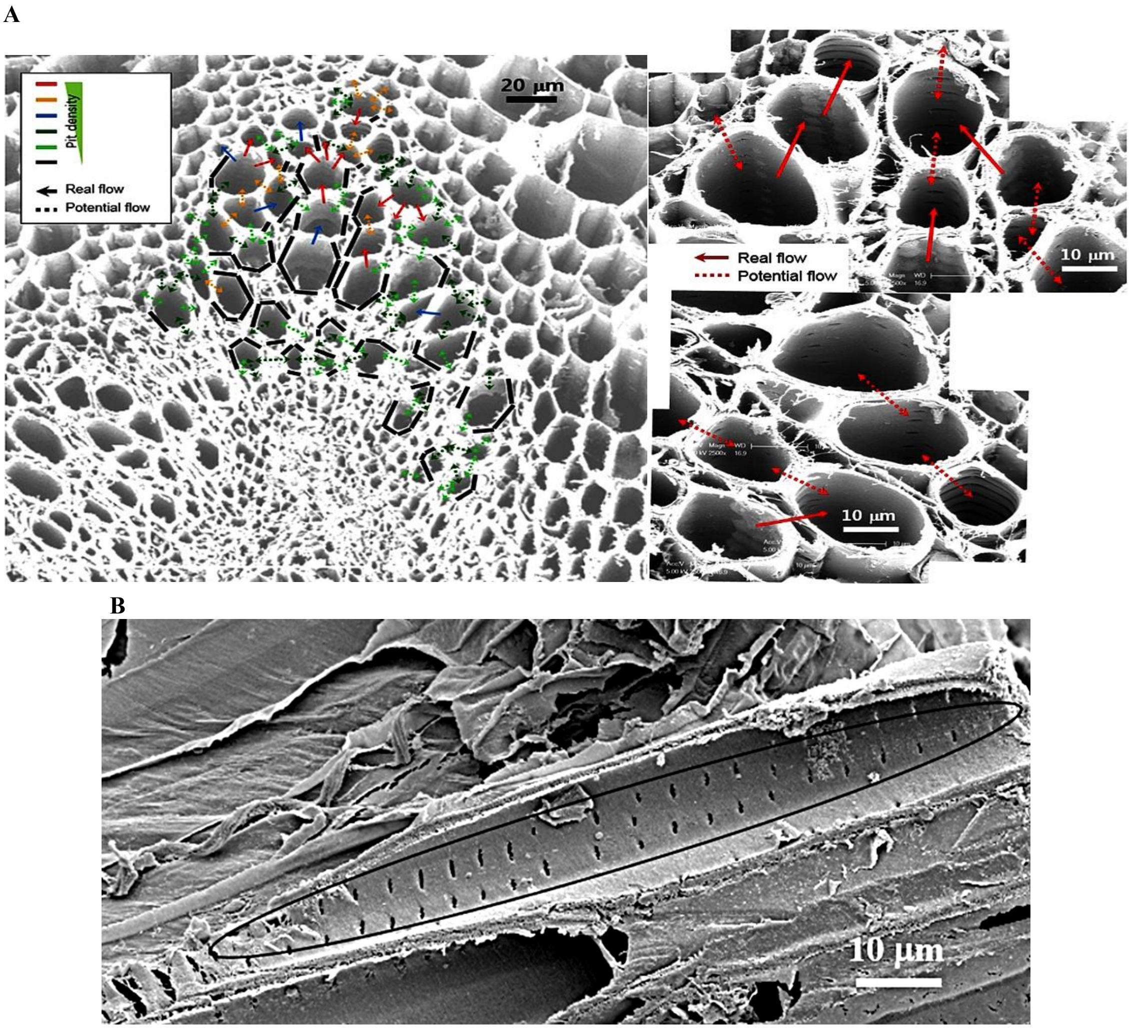

Figure A3. Morphology of vascular bundles obtained by SEM. **(A)** Xylems are in the form of bundles across the cross section. The vessels are interconnected through which water flows in the networked structures. **(B)** The longitudinally sectioned xylems. In addition to the typical axial flow, radial water flows are promoted by the interconnection among the adjacent xylems within a bundle. The radial flows are possible by the holes on the vessel walls through which water is transported.